JOURNAL OF PROPULSION AND POWER
Vol. 27, No. 2, March–April 2011

Experimental Transonic Centrifugal Compressor Investigation: Loading Effects on Deterministic Diffuser Velocity Fields

Beni Cukurel,* Patrick B. Lawless,† and Sanford Fleeter‡
Purdue University, West Lafayette, Indiana 47907

DOI: 10.2514/1.45697

The future of small gas turbines relies on higher-efficiency and higher-pressure-ratio centrifugal compressors for lighter, more efficient, and reliable designs. An efficient diffuser is essential to the performance, durability, and operability of a modern compressor stage. The diffuser entry flow in a high-speed centrifugal compressor is highly unsteady and complex, featuring shocks, boundary-layer/shock interactions, and large incidence variations imposed on the diffuser vanes. The observed flow structures are not only unsteady, but they are also strongly dependent on the steady compressor-stage loading. To characterize the variation in diffuser flow at different operating points of a modern transonic centrifugal compressor, particle image velocimetry experiments are conducted in the Purdue University high-speed centrifugal compressor facility. The data at all loading conditions demonstrated that the flowfield in the diffuser is characterized by a much more complicated structure than that associated with steady uniform diffusion. The semivaneless-space acceleration region's size is shown to be weakly dependent on loading, whereas the diffuser throat structures are strong functions of the loading condition.

I. Introduction

THE future of small gas turbines requires higher-efficiency and higher-pressure-ratio centrifugal compressors to lower specific fuel consumption, increase specific power, and increase the power-to-weight ratior. However, the complexity of the centrifugal compressor flowfield (specifically, in the impeller exit–diffuser inlet region) provides significant challenges to the design process, both for the diffuser and the impeller–diffuser matching.

The flow at the impeller exit is highly three-dimensional and possibly even partially separated. In an impeller passage, there are high- and low-momentum regions that are often referred to as the jet and wake in the literature. As the flow emerges from the impeller, the blade forces are lost and the jet and wake undergo a rapid mixing process in the vaneless space. Even though some earlier designers have assumed uniform flow due to this mixing in the circumferential direction downstream of the vaneless space, it has been shown that the mixing process does not suffice to reflect a homogeneous flow region [1]. On the contrary, the flow imposed on the vaned diffuser inlet is highly irregular. This complicated flowfield sweeps across the diffuser inlet, enforcing large unsteadiness on the overall flow in the vane passage.

The flow features in the vaned diffuser, especially in the inlet and throat regions, are far from a simple uniform homogenous diffusion process; there are shocks, boundary-layer/shock interactions [2], partial separation zones [3], varying inlet flow momentum, and incidence regions imposed on the diffuser vanes. In addition, there is a high degree of interaction between the impeller and diffuser that prevents accurate analysis as isolated components [4]. The effects of the diffuser geometry on the compressor stage are difficult to predict due to the existence of this coupling between the impeller and the diffuser. The potential field generated by the diffuser and imposed on the impeller exit is not only driven by the vane geometry, but is also dependent on the unsteady diffuser loading. This loading is in turn a function of the rotating impeller potential field and the highly three-dimensional velocity field produced by the impeller. These cross-dependencies are indicative of the difficulty in predicting the flow features in these machines, which enhances the value of available data to both performance and durability analyses.

Unfortunately, adequate steady and unsteady data that are representative of today's advanced high-speed compressors are limited in the open literature. This is partially due to the research emphasis on axial flow machines, but also to the difficulty of characterizing centrifugal compressor flowfields at realistic Mach numbers and pressures. Even though today's computational fluid dynamics codes do a fair job of characterizing the primary time-averaged flow features of the centrifugal compressor [5,6], there is clear need for high-resolution unsteady flow data for further advances. Better understanding of the diffuser flowfield is also crucial from a high-cycle-fatigue perspective, due to its effect on the diffuser potential field and thus on the forcing function observed by the impeller [7].

High cycle fatigue is a key issue, especially in the impeller trailing-edge region [8], due to the unsteady pressure fluctuations caused by the diffuser potential field [7], which is also a function of the flow structures present at the vane throat. It has been shown that these cyclic pressure variations imposed on the impeller trailing edge can be as strong in magnitude as the total steady pressure rise across the machine. The unsteady loading on the vaned diffuser of a low-speed compressor was also studied at various phase-locked impeller positions [9]. The results showed that the pressure fluctuations on the diffuser vane, due to both the impeller potential field and the unsteady flow caused by the nonuniformity of the impeller exit flowfield sweeping across the vane, created lift fluctuations as high as three times the steady lift.

Diffusers also have significance in operability limits of the compressor. The flow range of a centrifugal compressor is often limited by stall or choke of the vaned diffuser, with the most important portion of the diffuser being the semivaneless space between the leading edge and the throat of the diffuser vanes [2]. The blockage factor at the throat, which is also based on the diffusion from the leading edge of the blade to the throat, is the single-most-important parameter governing the channel diffuser recovery [10]. The vaned diffusers are highly sensitive to the mean and unsteady incidence imposed; specifically, the incidence on the vane suction surface is a significant parameter for diffuser performance [5] and stall [2].

Presented as Paper 2008-4699 at the 44th AIAA/ASME/SAE/ASEE Joint Propulsion Conference & Exhibit, Hartford, CT, 21–23 July 2008; received 6 June 2009; revision received 1 November 2010; accepted for publication 2 November 2010.

*Ph.D. Candidate, Mechanical Engineering. Student Member AIAA.
†Currently Senior Aerodynamics Engineer, Xcelaero Corporation. Associate Fellow AIAA.
‡McAllister Distinguished Professor, Mechanical Engineering. Fellow AIAA.

In a high-efficiency compressor that employs a vaned diffuser, if the flowfield in the diffuser is well understood [5], this allows potential for radial machines to have better performance, durability, and operability. Only through the detailed understanding and modeling of the physics of this region can we hope to enable better designs. Even though the effects of circumferential and spanwise variations on the diffuser flowfield at nominal loading have been characterized previously [11], empirical high-speed data capturing the flow physics associated with the impact of loading change on the diffuser flowfield is yet to be focused upon. Presented herein are particle image velocimetry (PIV) experiments that characterize the flow features in the diffuser passage of the Purdue University high-speed centrifugal compressor. This high-efficiency compressor features an impeller that produces a diffuser entry flowfield that is typical of modern transonic compressors. The flow characteristics are analyzed at midspan over a range of steady loadings at several relative impeller–diffuser positions. Since data are acquired only at a single spanwise location, the focus is on the diffuser flowfield variation in the circumferential direction, along with change in operating condition.

II. Technical Approach

A. Experimental Facility

The Purdue high-speed centrifugal compressor facility consists of an Allison 250-C30G turboshaft engine that drives the research compressor through a set of gear reductions. The centrifugal test compressor includes an advanced design 50° backsweep impeller that consists of 15 full and splitter blade pairs upstream of 22 wedge-type diffuser vanes. The ratio of the diffuser inlet radius to impeller exit radius is 1.094. The nominal operating speed of the compressor is 48,450 rpm. The geometry parameters of the research compressor are noted in Table 1.

The Purdue high-speed centrifugal compressor facility is instrumented with various steady temperature, pressure and optic probes to measure rotational speed, mass flow rate, pressure ratio and efficiencies. To change the speed of the test compressor, the C-30 engine output shaft speed is changed. The compressor is throttled with a butterfly valve at the exit of the outflow duct. The mass flow rate is calculated from the total and static pressures and the inlet total temperature measured with two rakes upstream of the test section. The pressure ratio PR is determined by ratio of the mass-averaged inlet total pressure and the mass-averaged exit total pressure calculated from the measurements by four three-headed total-pressure rakes distributed in four separate diffuser passages. The exit gas temperature is measured at the exit plenum. From the described measurements, the compressor's flow-pressure characteristic can be defined by the corrected speed and corrected mass flow rate.

B. PIV Velocity Measurements

PIV is an optical imaging technique that allows velocity fields in a flow to be measured. The flow is seeded with particles that track the fluid, and a planar laser light sheet is pulsed to illuminate these particles. An image of the particles is captured by a charge-coupled-device (CCD) camera perpendicular to the plane of the light sheet. A second laser pulse and exposure is made after a short time delay to extract a second image of the flowfield. During analysis, both these images are then divided into smaller sectors, called interrogation regions; and an average velocity within each interrogation region is determined by cross-correlation methods.

The PIV setup for this experiment consists of a Solo PIV Nd:YAG laser of 532 nm wavelength, a Hi-sense MKII CCD camera and Nikon Nikkor 35 mm focal-length camera lens. To synchronize the laser and the camera Dantec Dynamics Flow Manager version 4.71 software was used. This software also provided the necessary routines to process the PIV images. A Berkeley Nucleonics Corporation model 555 pulse delay generator is used to generate a phase lag to a once-per-revolution shaft trigger signal digitally generated by an Electro-Optical Product Corp. LT-850 laser tachometer. This allows data acquisition of different relative impeller–diffuser positions.

The seeding was introduced by a Topas model ATM 210/H aerosol generator using diethylhexyl sebacate seeding fluid. The diethylhexyl sebacate seeding-fluid particles have a mean diameter of 0.25 μm. A detailed analysis by Gallier [1] showed that they are small enough to track flow features as small as 0.5 mm up to 1.09% of the true velocity in regions bounded by the sonic velocity in the diffuser region. Clearly, for shock structures where the length scale is small (a few mean free paths), the error is considerably larger. Based on the above analysis, the "smearing" of the shock interface to a more finite length scale in the range of 10^{-4} m is thus expected.

C. Light-Sheet Design and Data Analysis

To illuminate the seeding particles in the flowfield, a thin planar light sheet is necessary. The difficulty in specifying the thickness of this plane comes from the fact that as the thickness of the light sheet increases, the cross-correlation among the particles becomes weaker since multiple seed particles from different spanwise locations appear in the images, thereby decreasing the signal-to-noise ratio. On the other hand, this planar thickness must be large enough to compensate for the motion of the particles in the third dimension for the time Δt between the consecutive images so that the particles appear in both images and can be correlated.

In most applications, the shape of the light-sheet plane is not important. However, in this application, to avoid reflections from the walls of the diffuser and the resulting inability to acquire PIV data, the light sheet had to track the diffuser walls, thus forming a triangular shape. For example, Fig. 1 shows an image acquired when a rectangular light sheet is imposed on the region of interest. Reflections dominate the image and it is not possible to extract any information. In contrast, Fig. 2 shows the raw image that is acquired with the light-sheet setup that follows the boundaries of the obstructions: i.e., the diffuser walls.

The final light sheet takes the form presented in Fig. 3. The outer lines indicate the planar view of the light sheet and the inner lines indicate the thickness associated with the plane at any given location.

Table 1 Research compressor parameters

Parameters	Values
Impeller	
Tip diameter	8.520 in. (21.65 cm)
Inlet diameter	5.6 in. (14.2 cm)
Number of blades	15 full and splitter pairs
Backsweep angle	50°
Nominal speed	48,450 rpm (clockwise, seen from inlet)
Diffuser	
Inlet diameter	9.320 in. (23.67 cm)
Exit diameter	13.6 in. (34.5 cm)
Axial passage width	0.545 in. (1.384 cm)
Number of vanes	22
Radial gap	1.094
Diffuser inlet vane angle	79.4°
Wedge diffuser opening angle	7.85°

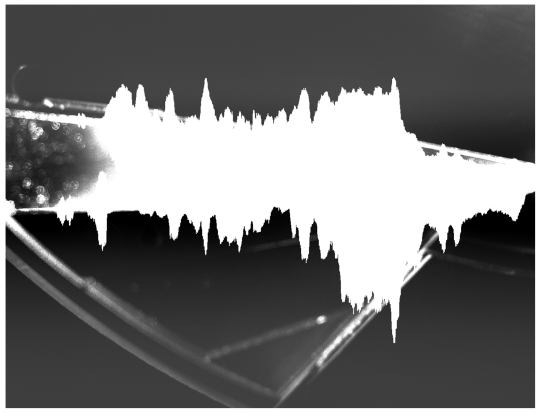

Fig. 1 Rectangular PIV light sheet.

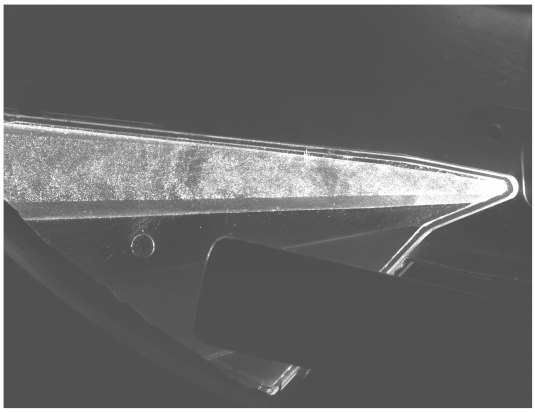

Fig. 2 Converging PIV light sheet with thickness tailoring.

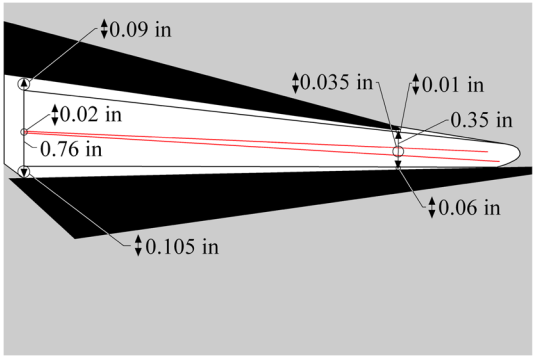

Fig. 3 Light-sheet plane and thickness in the diffuser.

Over 85% of the passage is successfully illuminated without compromising signal-to-noise ratio, due to reflections. The varying thickness of the light sheet, increasing in width, compensates for the highly three-dimensional flow in the inlet region, with the tracked particles not leaving the plane of interest. As the flow diffuses downstream, the velocities in the third dimension decrease, (not able to be measured in this configuration) enabling a smaller light-sheet plane thickness toward the exit, which improves the signal-to-noise ratio. In the throat region, the light-sheet thickness is approximately 0.035 in. and provides a cross section that is relatively insensitive to the motion of the particles in the third dimension. The light-sheet thickness downstream toward the diffuser exit is 0.02 in., which is typical for a relatively two-dimensional flowfield.

The apparent seeding particles seen in the raw images (Fig. 2) are diffraction-limited and thus larger than the actual particles (i.e., the size of the Airy disc rather than the particle). As the applied PIV method tracks centroids, this particle image distortion is not error-producing.

After acquiring the consecutive images with these particles present, a correlation routine extracts the flow velocity information. The correlation routine for locating these seeding particles consists of an advanced system called Adaptive Correlation provided in the Flow Manager software, which is an iterative multigrid approach with discrete window offset. In earlier analysis techniques such as cross-correlation, the interrogation-region size and maximum velocities observed within the flowfield are coupled:

$$V_{\max} \leq SN_{\text{int}} d_{\text{pixel}}/4 \tag{1}$$

where S is the scale factor, N_{int} is the integration region size, d_{pixel} is the pixel size, and Δt is the time associated with the lag between two consecutive images.

For the optical setup used in these experiments, $S = 12.804$, $N_{\text{int}} = 16$ pixels, $d_{\text{pixel}} = 6.45 \times 10^{-6}$ m/pixels, and $\Delta t = 10^{-6}$ s. Hence, the maximum allowable velocity in the region is 330.3 m/s. Velocities greater than this are subjected to the Nyquist criteria and mirrored in the spatial fast Fourier transform process associated with most correlation routines including cross-correlation. It is not possible to further decrease Δt to address this problem, as the minimum achievable Δt is 1 μs, due to hardware limitations. Not wanting to sacrifice spatial resolution by increasing the interrogation-region size, a superior analysis technique is necessary.

An iterative multigrid procedure with window offsetting tracks the local particle displacements with a large interrogation-region, allowing higher velocities, followed by a window offset in the second image for smaller interrogation regions in an iterative manner [12]. In other words, the analysis routine expects to find the second image seed particles in an interrogation-region location different from the initial one. This method enhances the accuracy, signal-to-noise ratio, minimum measurable displacement, maximum allowed displacement, and maximum measurable velocity, and the interrogation-region size are practically decoupled [13].

In the current analysis, raw images are subjected to an adaptive correlation routine with initial and final interrogation areas of 128×128 and 16×16 pixels respectively, with a 50% overlap applied among different regions. There are four grid refinement processes associated with this methodology. The zeroth Fourier coefficient of the image is eliminated (ac coupling) to remove the background noise at each step, as well as a peak validation routine. Peak validation compares the strength of the strongest correlation peak (which is assumed to be the true signal) with the second-highest peak (which is merely noise). The signal strength should exceed the noise; thus, if the signal-to-noise ratio is less than a certain threshold, the vector is rejected.

A local neighborhood validation technique is also commonly used with the multigrid analysis routines. It compares the vectors found with its 3×3 neighboring cells and allows vectors that are only below a user-defined velocity gradient. Since the spurious vectors that are not eliminated in the system would cause error propagation as the interrogation area gets smaller and smaller with each iteration, special attention must be paid in choosing the correct acceptance criteria. If it is chosen to be less than its optimum value for that flowfield, the analysis routine would be corrupted by the misconception of a more uniform flow. The error would propagate through all interrogation-region refinement steps. The result of this is similar to that of vector interpolation, with a smearing of the final solution. In this analysis, when the results compared with a solution that lacks such a filter, it is shown that only the excessively large obviously spurious vectors are removed from the solution. In this application, this is clearly the only goal for using such a technique, since it is known that the diffuser flowfield has large and varying velocity gradients, especially across the semivaneless space.

With the velocity information known at each interrogation region, the flow Mach number can be computed locally based on the plenum temperature; assuming an adiabatic process from the diffuser to the plenum, the total temperatures measured are equivalent to the total temperatures at the diffuser. For a given velocity and total temperature, the Mach number at every interrogation region is calculated by the local speed of sound in that area. The flow angles are calculated and are measured from the centerline of the diffuser passage and taken positive in the clockwise direction.

D. Error Analysis

Velocity measurement V is a function defined as $V = \hat{S}\Delta p/\Delta t$, where particle pixel displacement is Δp, optical magnification is $\hat{S}$, and the time delay between the two consecutive images is Δt. It was reported in [13] that the average measurement error for an interrogation analysis through cross-correlation with window offset was about 0.04 pixels. Assuming the maximum particle displacement of 4 pixels (one-fourth of the diameter of a 16×16 pixel interrogation window), this would imply a relative measurement error of 1%. In this setup, the optical magnification factor $\hat{S}$ is 8.259E − 5 m/pixel, which is established by comparing the images of a high-precision Max Levy DA039 line-grid ruler with the distances indicated by the grid. Considering the magnification factor,

Table 2 Data sets and loading conditions

Loading	Location	N_{cor}	$\dot{m}_{cor}$, lbm/s	PR (total to total)
A (lowest)	Midplane	$100.24 \pm 0.06\%$	5.0796 ± 0.021	3.890 ± 0.008
B	Midplane	$100.20 \pm 0.06\%$	5.0697 ± 0.020	4.045 ± 0.008
C	Midplane	$100.15 \pm 0.06\%$	5.0245 ± 0.020	4.240 ± 0.008
D	Midplane	$100.18 \pm 0.06\%$	4.9274 ± 0.019	4.397 ± 0.008
E (highest)	Midplane	$100.41 \pm 0.06\%$	4.6708 ± 0.018	4.485 ± 0.008

the grid lines appear 0.92 pixels wide through the CCD camera; thus, the scale is known to within a pixel. Using this information, the uncertainty due to optical magnification is 0.41%. In this experiment, the time delay between the two consecutive images is the minimum allowed by the hardware limitations, $\Delta t = 10^{-6}$ s. The architecture of integrated circuits such as found on a computer board may introduce fluctuations in the time delay, on the order of 1 ns. Thus, the uncertainty associated with the time delay can be calculated as 0.1%. The total uncertainty in the velocity measurements based on the experimental setup is dominated by the particle displacement measurement error. For the above considerations the velocity uncertainty is equal to 1.08%. The uncertainty in Mach number, based on velocity uncertainty and uncertainty in total temperature, is on the order of 2.8%.

E. Experimental Conditions

In this experiment, the diffuser flowfield in the Purdue centrifugal compressor has been investigated using PIV. Tests are conducted in the vaned diffuser at midspan for five relative diffuser–impeller positions, with the impeller full-splitter blade passage pair divided into five equally spaced phase delays, referred to as delay 0, delay 1, delay 2, delay 3, and delay 4. The data presented are ensemble-averaged with 200 images and a local minimum of 25 valid time instances for each vector flowfield map. The velocity measurements are conducted at various operating points on the throttle line given in Table 2. When these steady loading conditions are compared with the compressor 100% speed line [14]: loading A is the low loading operating point, loading B is on the choke line, loading C is nominal (close to the design operating) condition, loading D can be considered high loading, and loading E is the prestall loading condition.

III. Results

A. Vaneless Space: Diffuser Inlet Flow

Typical vaneless-space Mach numbers reported by Gallier [1] for 90% speed line in the vaneless space, along with exemplary diffuser data gathered in this investigation at 100% speed, are shown in Fig. 4 for a single vane-relative impeller position. Even though Gallier's [1] investigation was conducted at lower speed, it is sufficient to give a characteristic interpretation of the flow features imposed on the diffuser. For illustrative purposes, local flow vectors, shown as black arrows superimposed on the contour plot, are drawn to be representative of flow direction and are scaled to the local Mach numbers. The suction and pressure surfaces of the vanes and blades are indicated with an S or P, respectively.

At nominal loading conditions, the impeller exit flowfield at midspan demonstrates regions of high and low relative momentum that Dean [10] referred to as the jet and wake. The wake region, concentrated mainly on the suction side, is described in the rotating frame of reference by low relative Mach numbers. Because of the high tangential component imposed by the wheel speed, in the fixed frame of reference, this region demonstrated the highest absolute Mach numbers with near tangential flow angles. The jet region, concentrated in the impeller pressure side, is a high-momentum region in the relative frame, but similarly, it is observed in the fixed frame as a low-momentum region, mostly in the radial direction.

Region A indicates the impeller jet flow characteristics imposed on the diffuser suction-side wall, with highly radial flow angle and lower momentum, as expected. Region B shows the approach of the impeller wake toward the diffuser suction-side wall. Once again considering the velocity triangles, a low-momentum region in the impeller reference frame is a high-momentum region with low flow angle for the diffuser. Because of the impingement of regions A and B, the diffuser suction-side acceleration region forms, represented by region C. This is the flowfield where the Mach number is near $M = 0.9$, just below the critical Mach number. For the given impeller–diffuser geometry, 30 full and splitter blades and 22 vanes, there are approximately 1.35 blade passages imposed on the diffuser inlet at any given time. For the delay shown, there is impingement of yet another impeller jet on the semivaneless-space region just before the diffuser throat, region D. In the prethroat region E, the flow coming from the upstream portion of the vane with higher momentum, regions B and C, interacts with the low-momentum region of the impeller jet (region D).

As the fluid enters the throat, it accelerates due to area reduction. Downstream of the throat, region F, the flow transitions supersonic to

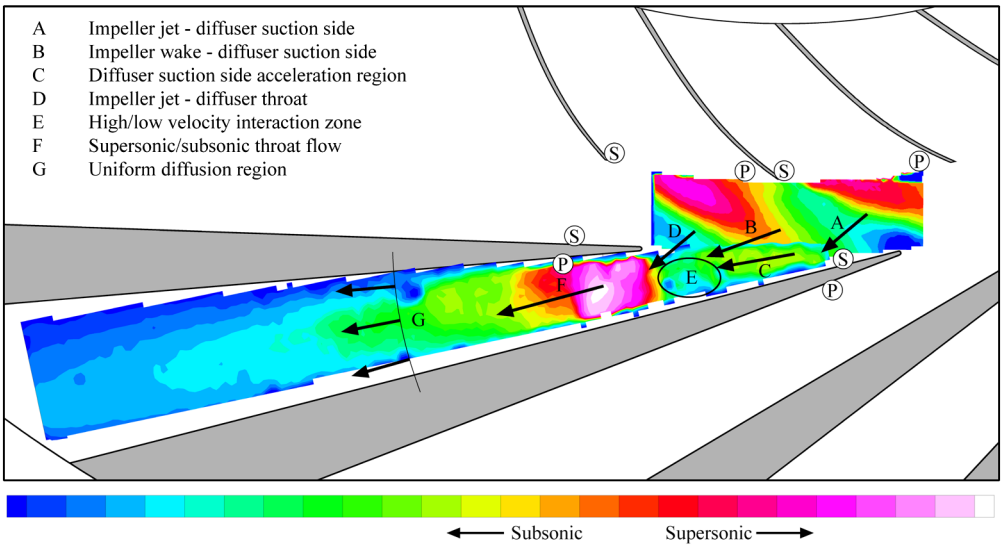

Fig. 4 Impeller flow interaction with the diffuser.

subsonic. Further downstream, there is a more uniform diffusion region, represented by region G.

The flow features described above for a single vane-impeller position are clearly subject to the unsteady forcing function created by the impeller exit flowfield. This interaction needs to be analyzed for various loading conditions and over a full interaction cycle to characterize the complete unsteady diffuser flowfield.

B. Flow Variation in the Diffuser

The midspan Mach numbers and flow angles at various loading conditions for different delays are given in Figs. 5–14. The results at each delay are stacked such that loading A is at the lowest compressor pressure rise and loading E is at the highest. Note that the operating conditions A and B are on the choke line, loading C is the nominal loading condition, and loadings D and E are at a lower flow rate. Throughout these results, the lower diffuser surface appearing in the figures is identified as the suction side and the upper surface is referred to as the pressure side. In actual operation, the behaviors of these surfaces change with loading, with the notation specified above that typical of a higher loading condition. The flow angles presented are measured from the centerline of the diffuser passage and taken positive in the clockwise direction.

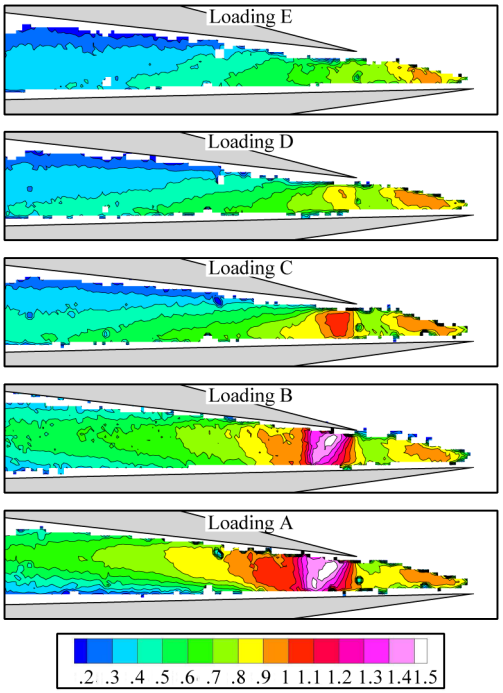

Fig. 5 Loading variation, Mach number, delay 0.

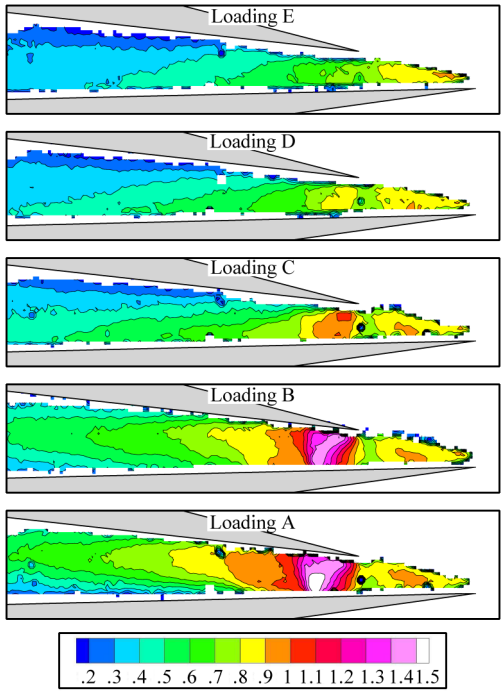

Fig. 7 Loading variation, Mach number, delay 1.

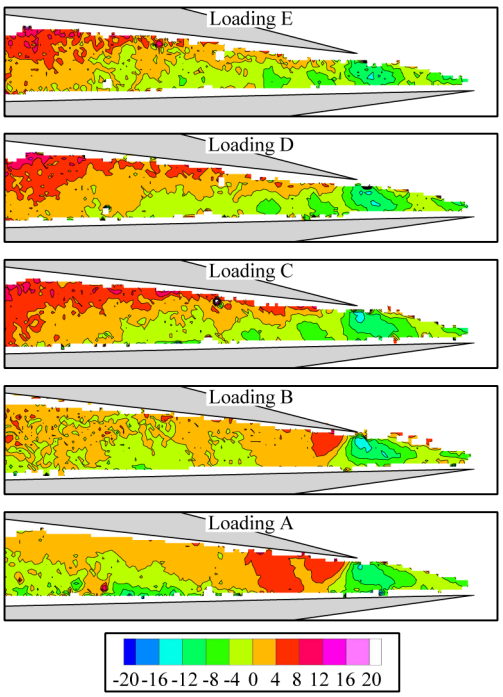

Fig. 6 Loading variation, flow angle, delay 0.

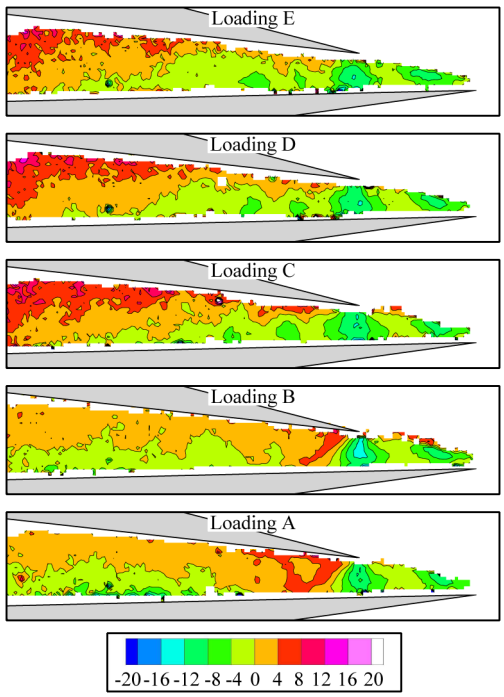

Fig. 8 Loading variation, flow angle, delay 1.

In Figs. 5 and 6, the flow Mach numbers and flow angles can be seen for all five loading conditions at delay 0. First, the global variation in flow due to change in loading should be focused upon. The overall Mach numbers at lower loading conditions such as A and B are significantly higher than the further throttled operation points. This is simply an artifact of the reducing mass flow rates as the compressor stage is throttled. Another important feature that can be observed when increasing throttle from loading B to C is that, with the changing incidence, the vanes have reversed their suction and pressure sides. There are also significant variations with loading in the throat region, which are mainly caused by the changes in the diffuser inlet flow.

1. Flow in the Semivaneless Space

In all loading conditions, there is a Mach number increase just downstream of the leading edge of the vane suction surface, in what is termed the semivaneless space. The semivaneless space consists of the triangular region restricted by the suction-side leading edge, pressure-side leading edge, and diffuser throat. The main effect of the impeller-generated unsteadiness is seen in this region. The Mach number is approximately 0.9 in this region, observed for all loading conditions and delays. This is in agreement with the design criteria outlined by Pampreen [15], which suggests that designers avoid supersonic flows in this region, thereby avoiding prethroat shock structures and their adverse effects on boundary-layer growth. This

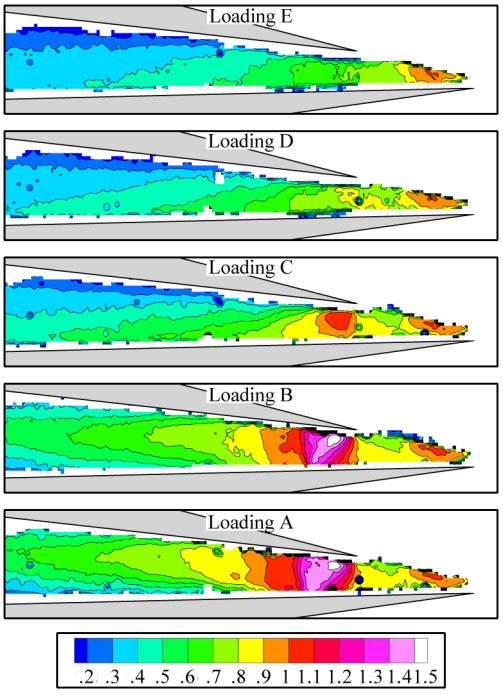

Fig. 9 Loading variation, Mach number, delay 2.

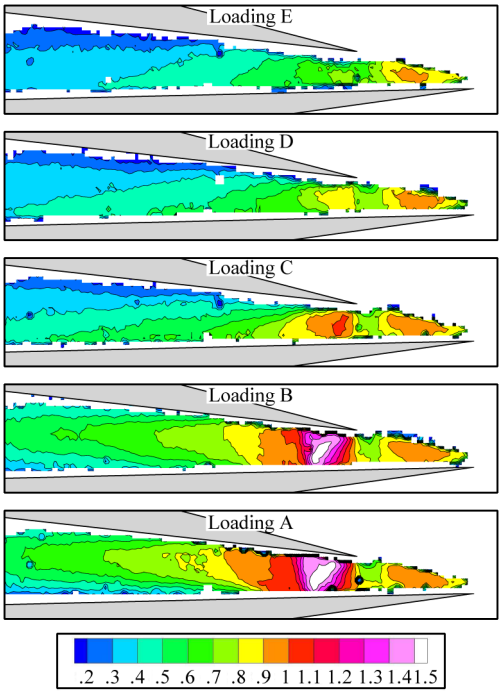

Fig. 11 Loading variation, Mach number, delay 3.

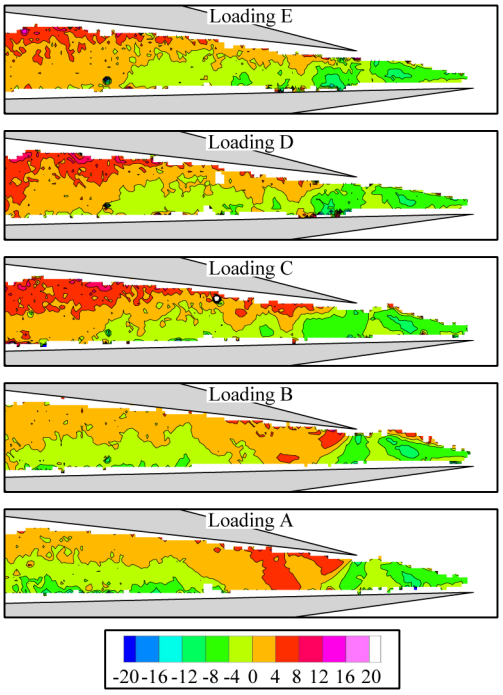

Fig. 10 Loading variation, flow angle, delay 2.

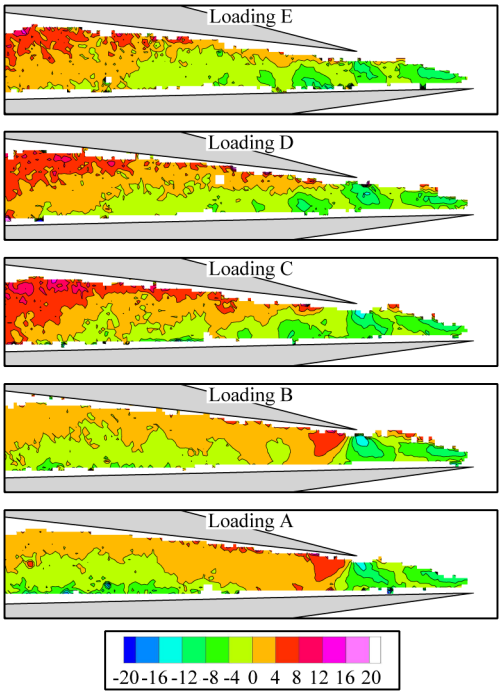

Fig. 12 Loading variation, flow angle, delay 3.

region is consistent with a blockage-driven acceleration of the flow about the suction side of the diffuser. The semivaneless-space acceleration region's size is weakly dependent on loading, reflecting a slight reduction in size with increased loading; this behavior is observed for all delays. The location of this increased Mach number region is completely independent of loading for any given relative impeller position, as shown by comparing delay 0 (Fig. 5) with other delays (Figs. 7, 9, 11, and 13). Both the size and the location of the semivaneless-space acceleration region are strong functions of the relative impeller position. The impingement of jet and wake at different portions of the semivaneless space creates this variation. This type of circumferential variation and its effects on diffuser flowfield are best observed in flow-angle contours.

In Fig. 6, delay 0, the low flow angles appearing in the semivaneless space, approximately −14°, reflect the effect of the jet flow on the diffuser near the pressure-side leading edge. Upstream of the upper-vane leading edge, immediately after the semivaneless-space acceleration region (Fig. 5), the flow decelerates, where the Mach number changes from 0.85 to 0.75 before the throat is reached. The behavior of the flow in this region is partly a function of the area increase with increased radius. But, especially for the nominal and lower loading conditions, the main cause is believed to be due to the jet flow associated with low Mach numbers, characterized by the large negative-flow-angle region described in Fig. 6, interacting with the suction-side acceleration region, identified by a locally higher Mach number in the semivaneless space (Fig. 5). The inhomogeneous flow character in the diffuser inlet (high-momentum flow with lower incidence and low-momentum flow with higher incidence) creates a rapid adjustment zone where these two flowfields interact, identified by the locally lower Mach number region upstream of the throat. This region is a direct result of the impeller jet fluid; thus, the intensity of this interaction region characterized by a deviation in flow Mach number is a function of the strength and impingement location of the impeller jet fluid on the diffuser semivaneless space. For example, for the same relative impeller positions at loadings A and B, in Fig. 5, where the mass flow rate is approximately the same, due to the operating condition where the throat has sonic flow, the intensity of this interaction region is greater for loading B, indicated by a slightly larger Mach number reduction region in the prethroat flow. Specifically, the approach Mach at loading A appears to be more atypical in comparison with loading cases B and C. Thus, although the diffuser is observed to reach a sonic condition at throat midspan measurement plane, it does not demonstrate complete isolation from downstream conditions. In addition, in loading A, the adjustment-zone Mach numbers do not seem to vary as much from the mean flow, in agreement with the smaller and less negative flow angles, as observed in Fig. 6.

For higher loading conditions (loadings D and E), the decrease in Mach number downstream of the semivaneless-space acceleration region is more of an artifact of the reduction in overall mass flow rate and thus global reduction in Mach numbers. For operating conditions away from the choke line, similar diffuser inlet flow structures are observed at all loading conditions. Comparing these finding with other delays (Figs. 7, 9, and 11), similar trends are observed for any given impeller position at all delays except for delay 4 (Fig. 13), where there is no rapid adjustment zone for any loading condition for this delay. To further identify the changes in this interaction zone with relative impeller–diffuser positions, thus varying the impingement location of the impeller jet, at a give loading condition, different relative impeller–diffuser positions should be compared. In Figs. 7, 9, and 11 it is possible to see that the size and strength of this prethroat adjustment zone vary significantly with relative impeller positions. This is due to the change of location where the impeller jet is impinged upon on the lower diffuser-vane surface. Note that in delay times where there is a clear adjustment zone upstream of the throat, such as delays 0 and 3 (Figs. 5 and 11), the flow angles near the pressure-side leading edge are depressed, reflecting the impact of the impeller jet in the prethroat (Fig. 12).

On the other hand, for delay 4, there is no apparent adjustment region indicated by the locally lessened Mach numbers in the prethroat region. Instead, more uniform extended semivaneless-space acceleration is visible, merging with the throat flowfield (Fig. 13). This is also seen by the lack of large negative-flow-angle regions in the prethroat region (Fig. 14), suggesting a weakened or absent impeller jet flow (and thus the lack of an adjustment zone) in the prethroat region. Note that in this specific impeller–diffuser position, the overall Mach numbers observed at the throat are lower than those at other delays (Fig. 5). This result is especially visible for loading C; the flow is fully subsonic in Fig. 13.

A similar occurrence is observed at delay 2. The rapid adjustment zone upstream of the throat leading edge is much weaker than observed for other delays. There is an early sharp rise in Mach number near the leading edge, followed by a more uniform extended

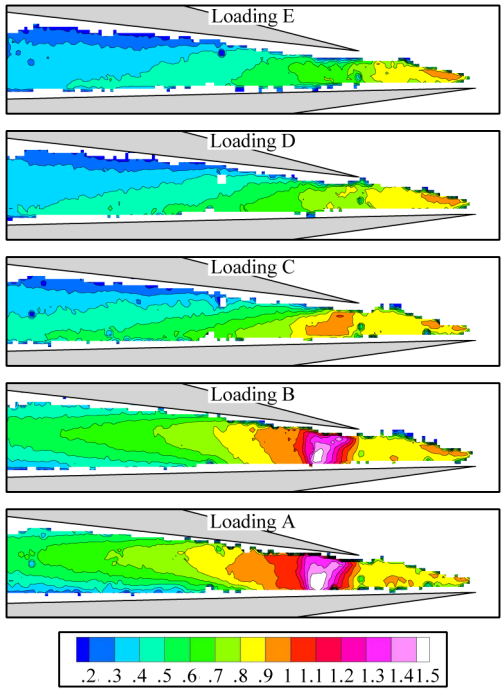

Fig. 13 Loading variation, Mach number, delay 4.

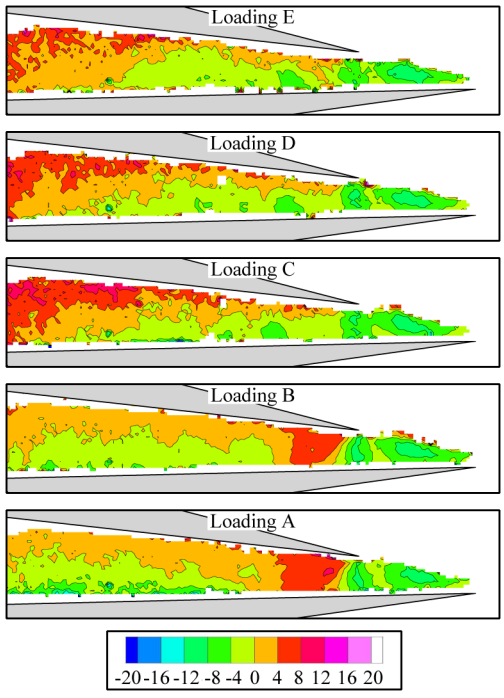

Fig. 14 Loading variation, flow angle, delay 4.

semivaneless-space flowfield. When compared with the flow angle for this delay, the large negative flow angle imposed by the jet flow ceases to exist. But the main difference between these two delays is the existence of a high Mach number region in delay 2 in the lower-vane leading-edge region. This is an expected artifact of the impeller wake flow dominance in the diffuser inlet. Contrary to delay 4, in delay 2, the Mach numbers observed at the throat are not smaller than those observed for any other delay.

From the perspective of loading variation, at delays 2 and 4, in the prethroat region, the incidence angles for all operating conditions are quite similar. However, the throat and downstream flow Mach numbers are expectedly different at the various loading conditions, with the exception of loadings A and B. This is because the flow is driven almost solely by the mass flow rate at these delays: hence, the flow structure similarity at loadings A and B. For the rest of the loading conditions, there is a scaling effect with respect to mass flow rate that changes the diffuser inlet flow in an absolute sense, but it does not seem to affect the qualitative flow structure behavior, as can be seen by the similarity in flow angles at semivaneless space for all loading conditions (Figs. 10 and 14). But due to the change in inlet Mach numbers, at different loading conditions the throat structures show differences.

In general, the circumferential variation in the suction-side acceleration region seems to be equally strong at all loading conditions, for all delays, and driven by the location of the impeller jet.

2. *Flow in the Diffuser Throat*

As the compressor is moved toward the choke line, the mass flow rate increases, resulting in variations in throat flow features. At loadings A and B, for all delays, around the throat region, it is possible to see indications of oblique shock types of structures, followed by a normal shock in the Mach contours. Figure 15 presents the Mach numbers and flow angles in the diffuser throat region for a typical delay at midspan around loading B on the choke line. The streamlines are superimposed on the data to provide a better understanding of the flow structures.

Immediately downstream of the upper-vane leading edge, there is an acceleration region where the Mach numbers increase until a value of approximately 1.4 is reached. The flow-angle data show that the acceleration region is also associated with flow turning of approximately 8°.

The process that allows this increase in supersonic flow velocity along with the turning can be characterized by a set of expansion waves, originating about the vane leading edge. This is in agreement with the area increase. As an expected feature of the expansion fan, the flow is turning away from itself, in the clockwise direction (in this case, approximately 8°). Downstream of the high Mach number observed, there is a region of supersonic deceleration as well as a flow turning associated with that region. The flow decelerates from Mach 1.4 to approximately 1.2 in a very short distance. This can be explained by an oblique shock. The angle between the oblique shock wave front and the inlet flow, $M_i = 1.4$, to this wave front is the shock angle β, $\beta = 56°$. For the temperatures at the diffuser, approximately 850°R, the specific heat ratio γ is approximately 1.39. From the 1-D compressible flow relations, the wedge angle θ, which represents the change in flow angle due to the oblique shock in this case, is 6.7°, calculated from

$$\tan\theta = 2\cot\beta\left[\frac{M_i^2\sin^2\beta - 1}{M_i^2(\gamma + \cos 2\beta) + 2}\right] \tag{2}$$

In Fig. 15, the flow is turning into itself, counterclockwise direction, as expected through an oblique shock (in this case, approximately 6°); this is in agreement with the calculations. The Mach number downstream of the oblique shock is $M_e = 1.13$, calculated from

$$M_e^2 = \frac{M_i^2\sin^2\beta + [2/(\gamma - 1)]}{\sin^2(\beta - \theta)\{M_i^2\sin^2\beta[2\gamma/(\gamma - 1)] - 1\}} \tag{3}$$

Comparing the calculations with the figure, the region that the flow turning stops is approximately Mach contour 1.1. This indicates a fairly strong oblique shock effect. Immediate downstream of the oblique shock, a region of lower Mach supersonic flow is visible. A normal shock appears as a structure perpendicular to the channel centerline. For a normal shock with an inlet Mach number of 1.13, the subsonic outflow Mach number is approximately 0.89; in agreement with the flow Mach numbers observed downstream of the normal shock.

As the mass flow rate decreases with increased loading (loading C), there is only a barely supersonic region (subsonic in delay 4), followed by uniform diffusion. The throat shock structures for this loading are clearly different from in the choke loading. For a

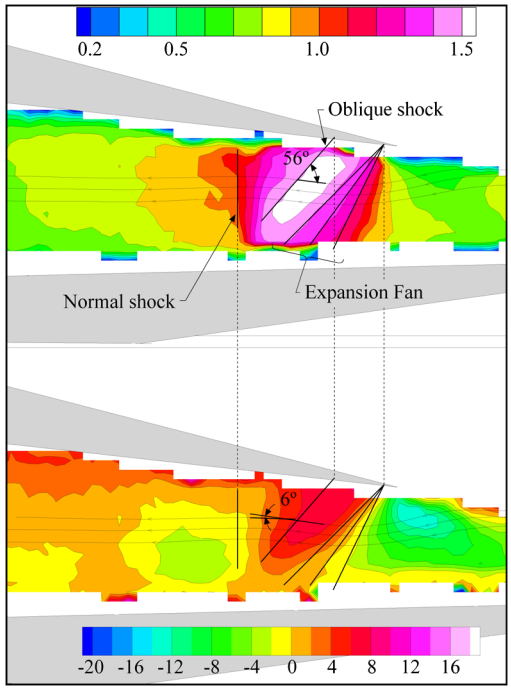

Fig. 15 Choke loading, throat shock structures.

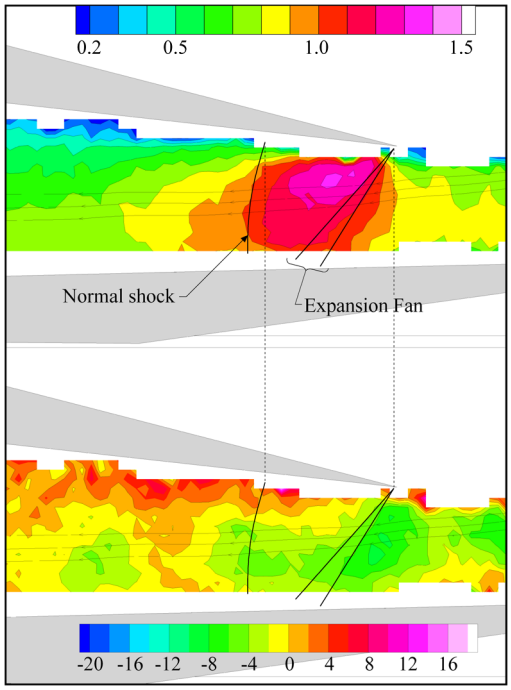

Fig. 16 Nominal loading, throat shock structures.

typical delay at midspan, Fig. 16 represents the Mach numbers and flow angles seen at the throat. Similar to the lower loading case, there is a clear supersonic acceleration region associated with the expansion fan that originates from the upper-vane leading edge. The turning at this region is also indicative of this phenomena. In nominal loading (loading C), due to lower mass flow rates and the less aggressive flow angles imposed on the upper-vane leading edge, the Mach number in the throat increases only up to approximately 1.25. This region is followed by a mild supersonic deceleration and finally by a normal shock that brings the flow down to subsonic velocities. Note that the initial deceleration of the flow is rather slow, indicated by more spread out Mach contours and is not associated with a flow-angle change. The normal shock seems to occur as a curved structure, approximately perpendicular to the diffuser walls.

At higher loading conditions (loadings D and E), the flow appears to be subsonic throughout the diffuser. Even though the compressor is further throttled from loading D to E, the flowfields associated with the diffuser appear to have strikingly similar Mach contours, except for a slightly higher Mach number, approximately 0.1, in the throat region for loading D. Especially in delay 4, there appears to be no appreciable difference between loadings D and E. It is possible that this is due to a redistribution of the flow in the spanwise direction as the compressor reaches its operability limits, [16]. Thus, even though loading E has less overall mass flow than loading D, locally at midspan, the Mach number contours suggest comparable flow Mach numbers and thus mass flow rates.

The throat shock structures observed not only vary with loading but also in the circumferential direction with impeller position. At loading conditions that are representative of nominal loading or less (loadings A–C), it is possible to observe that the locations vary at which maximum Mach numbers occur in the throat, dependent upon the diffuser inlet flow. For example in delay 2, the maximum Mach number in the throat region occurs about the upper vane. On the contrary, in delay 4, the higher Mach numbers in the throat appear about the lower vane. This type of spatial Mach number variation in the throat is partially an artifact of the three-dimensional flow characteristic observed in the diffuser inlet that is not captured in this study [16]. On the other hand, in delay 3, the Mach numbers in the throat seem to be more consistent with a two-dimensional flowfield, observed by the uniformity in Mach numbers in the throat region within each loading condition.

Overall, in the throat region, the circumferential variation decreases at higher loading conditions. For higher loading conditions, this is observed by the lack of change in throat flow structures in the circumferential direction, when compared with their lower loading counterparts. Because the impeller discharge flow is formed of jet and wake types of features, with each one having its own characteristic, the impeller jet flow reduces in size as the loading increases, and the flow approaches a more uniform character.

3. *Flow Downstream of the Throat*

Flow downstream of the throat reflects a diffusion process that does not have any circumferential variation, as would be observed by comparing the Mach numbers for a given loading at various delays. The uniformity of this diffusion is debatable, since the acquired data are impeller-phase-locked and ensemble-averaged. There may be perturbations that are inherent to the system and are being shed with their own discrete frequencies. The only certain conclusion is that there are no impeller-phase-locked occurrences downstream of throat. This shows that the impeller-phase-locked flow unsteadiness downstream of the throat decays rapidly, reflecting a more homogenous flow region. As the loading is increased, the Mach numbers observed in the postthroat region scale with the reduced mass flow rate, and at high loading conditions (loadings D and E), there are regions with flow velocities as low as Mach 0.3 in the aft diffuser regions. Observing the flow angles at these locations, we can conclude that the upper vane at these high loading conditions is aerodynamically the pressure side; thus, these low Mach number regions are not indicative of a separation at the midspan measurement plane.

IV. Conclusions

This study has provided detailed phase-resolved velocity data quantifying the effect of compressor-stage loading on the flow through the diffuser of the Purdue centrifugal compressor, accomplished using particle image velocity (PIV) technique. These unique data build on previous investigations in this facility on the vaneless space and diffuser flowfields. The data at all loading conditions demonstrated that the flowfield in the diffuser is, as expected, characterized by a much more complicated structure than that associated with steady uniform diffusion. Although mixing clearly occurs in the vaneless space, these data show that strong momentum variations still exist in the circumferential direction in the diffuser.

The semivaneless-space acceleration region's size is shown to be weakly dependent on loading, reflecting a slight decrease in size with increased loading. The location of this increased Mach number region is independent of loading variation for any given relative impeller position. Both the size and the location of the semivaneless-space acceleration region are strong functions of the relative impeller position. The impingement of jet and wake at different portions of the semivaneless space creates this variation. Circumferential variation in the suction-side acceleration region seems to be equally strong at all loading conditions and driven by the location of the impeller jet.

Diffuser throat structures were shown to vary significantly with loading. Near the choke line, the flow accelerates to supersonic Mach numbers, then is shown to adjust to subsonic flow through an oblique shock and then a normal shock. A further increase in the loading results in a more mild supersonic flow and an adjustment to subsonic flow through a normal shock. As the mass flow is further decreased, the entire diffuser flowfield becomes subsonic. The diffuser throat flow structures also vary with different impeller–diffuser relative positions. Over a part of the cycle for most loading conditions, the semivaneless-space acceleration-region Mach numbers decreased and the prethroat high- and low-momentum fluid interaction regions shifted upstream toward the semivaneless space, while decreasing in size and strength. This variation in the diffuser inlet flow caused changes in the throat flow structures. At a given measurement location and loading, when the throat shocks existed, they were slightly different and there were variations in the upstream and downstream Mach numbers, due to the unsteadiness in the diffuser inlet. However, for most loading conditions, the flow downstream of the throat was relatively unaffected by the impeller motion.

Acknowledgment

This research was funded in part by the Rolls-Royce Corporation. This support is most gratefully acknowledged.

References

[1] Gallier, K., "Experimental Characterization of High Speed Centrifugal Compressor Aerodynamic Forcing Functions," Ph.D. Dissertation, Mechanical Engineering Dept., Purdue Univ., West Lafayette, IN, 2005.

[2] Senoo, Y., *Vaned Diffusers*, von Karman Institute for Fluid Dynamics, Rhode-St-Genèse, Belgium, 1984.

[3] Krain, H., *Experimental Observation of the Flow in Impellers and Diffusers*, VKI Lecture Series 1984–2007, von Karman Institute for Fluid Dynamics, Rhode-St-Genèse, Belgium, 1984.

[4] Inoue, M., and Cumpsty, N. A., "Experimental Study of Centrifugal Impeller Discharge Flow in Vaneless and Vaned Diffusers," *Journal of Engineering for Gas Turbines and Power*, Vol. 106, 1984, pp. 455–467. doi:10.1115/1.3239588

[5] Boncinelli, P., Ermini, M., Bartolacci, S., and Arnone, A., "Impeller–Diffuser Interaction in Centrifugal Compressors: Numerical Analysis of Radiver Test Case," *Journal of Propulsion and Power*, Vol. 23, No. 6, 2007, pp. 1304–1312. doi:10.2514/1.27028

[6] Dorney, D. J., Roger, L., and McLaughlin, D. K., "Numerical Simulations of Flows in Centrifugal Turbomachinery," *Journal of Propulsion and Power*, Vol. 11, No. 5, 1995, pp. 899–907. doi:10.2514/3.23915

[7] Sanders, A. J., and Fleeter, S., "Potential Field Interactions in a Low-Speed Centrifugal Compressor," *Journal of Propulsion and Power*,

Vol. 14, No. 6, 1998, pp. 925–933.
doi:10.2514/2.5386

[8] Arndt, N., Acosta, A. J., Brennen, C. E., and Caughey, T. K., "Experimental Investigation of Rotor-Stator Interaction in a Centrifugal Pump with Several Vaned Diffusers," *Journal of Turbomachinery*, Vol. 112, No. 1, 1990, pp. 98–108.
doi:10.1115/1.2927428

[9] Arndt, N., Acosta, A. J., Brennen, C. E., and Caughey, T. K., "Rotor-Stator Interaction in a Diffuser Pump," *Journal of Turbomachinery*, Vol. 111, No. 3, 1989, pp. 213–221.
doi:10.1115/1.3262258

[10] Dean, R. C., *The Fluid Dynamic Design of Advanced Centrifugal Compressors*, VKI Lecture Series 66, von Karman Institute for Fluid Dynamics, Rhode-St-Genèse, Belgium, March 1974.

[11] Cukurel, B., Lawless, P. B., and Fleeter, S., "PIV Investigation of a High Speed Centrifugal Compressor Diffuser: Circumfrential and Spanwise Variations," 43rd AIAA/ASME/SAE/ASEE Joint Propulsion Conference & Exhibit, Cincinnati, OH, AIAA Paper 2007-5021, July 2007.

[12] Scarano, F., and Riethmuller, M. L., "Iterative Multi Grid Approach in PIV Image Processing with Discrete Window Offset," *Experiments in Fluids*, Vol. 26, No. 6, 1999, pp. 513–523.
doi:10.1007/s003480050318

[13] Westerweel, J., Dabiri, D., and Gharib, M., "The Effect of a Discrete Window Offset on Accuracy of Cross-Correlation Analysis of Digital PIV Recordings," *Experiments in Fluids*, Vol. 23, 1997, pp. 20–28.
doi:10.1007/s003480050082

[14] Carnell, W. F., "Aerodynamic Performance and Forcing Function Measurements in a High-Speed Centrifugal Compressor," M.S. Thesis, Purdue Univ., West Lafayette, IN, 2002.

[15] Pampreen, R. C., "The Use of Cascade Technology in Centrifugal Compressor Vaned Diffuser Designs," *Journal of Engineering for Power*, Vol. 94, No. 3, 1972, pp. 187–192.
doi:10.1115/1.3445671

[16] Cukurel, B., Lawless, P. B., and Fleeter, S., "Particle Image Velocity Investigation of a High Speed Centrifugal Compressor Diffuser: Spanwise and Loading Variations," *Journal of Turbomachinery*, Vol. 132, Paper 021010.
doi:10.1115/1.3104616

C. Tan
Associate Editor